

SUPPLEMENTARY MATERIAL

Ultraviolet dielectric hyperlens with layered graphene and boron nitride

Junxia Wang^{1,2}, Yang Xu^{1, 4, a)}, Hongsheng Chen^{1,2,4, b)}, and Baile Zhang^{3, c)}

1Department of Information Science and Electronic Engineering, Zhejiang University, Hangzhou 310027, China

2The Electromagnetics Academy at Zhejiang University, Zhejiang University, Hangzhou 310027, China

3Division of Physics and Applied Physics, School of Physical and Mathematical Sciences, Nanyang Technological University, Singapore 637371

4Cyrus Tang Center for Sensor Materials and Applications, Zhejiang University, Hangzhou 310027, China

a) yangxu-isee@zju.edu.cn

b) hansomchen@zju.edu.cn

c) blzhang@ntu.edu.sg

Kramers-Kronig relations

The Kramers-Kronig relations [S1] are applied to post-process the result from the first principle simulation. By the principle of causality, the relative permittivity $\varepsilon(\omega) = \int_0^\infty \varepsilon(\tau) e^{i\omega\tau} d\tau$ is seen to be an analytic function of the complex variable ω on the upper half plane. From the defining equation of $\varepsilon(\omega)$, we see that $\varepsilon^*(\omega) = \varepsilon(-\omega)$. Separating into real and imaginary parts, we have $\varepsilon_R(\omega) = \varepsilon_R(-\omega)$ and $\varepsilon_I(\omega) = -\varepsilon_I(-\omega)$. By Cauchy's theorem, we find the causality condition, i.e. the Kramers-Kronig relations, as follows

$$\varepsilon_R(\omega) - \varepsilon_\infty = \frac{1}{\pi} PV \int_{-\infty}^{\infty} d\alpha \frac{\varepsilon_I(\alpha)}{\alpha - \omega}, \quad (1)$$

$$\varepsilon_I(\omega) = -\frac{1}{\pi} PV \int_{-\infty}^{\infty} d\alpha \frac{\varepsilon_R(\alpha) - \varepsilon_\infty}{\alpha - \omega}, \quad (2)$$

Where $\varepsilon_\infty = 1$ in our work. With the imaginary part of the relative permittivity from the first principle simulation and the *f*-sum rule fulfilled, we can use the discrete form of the Kramers-Kronig relations in Eq. (1) to derive the real part of the relative permittivity, and then

derive the imaginary part of the relative permittivity in Eq. (2), serving as a cross check of the quality of the Kramers-Kronig transformation.

The dielectric tensor of monolayer graphene for different polarized waves

The optical properties of monolayer graphene, shown in the manuscript, are basically in agreement with the results in Ref. [17].

The optical properties of graphene in Ref. [17] are obtained using VASP (Vienna Ab initio simulation package) code, implementing the PAW formalism [S2]. They have used the PBE exchanged-correlation functional [S3]. To ensure negligible interaction between periodic images, a large value (20 Å) of the cell parameter was used. The convergence of the dielectric function was obtained by using $80 \times 80 \times 5$ Monkhorst-Pack mesh [S4]. For the plane wave expansion of the wave function a 400 eV cut-off was used. The LDA and GGA functionals do not capture the effects of the van der Waals interaction between the graphene planes. Because they focus on the dielectric function within the graphene planes, LDA and GGA are expected to be accurate. Their dielectric function of monolayer graphene is shown in Fig. S1(a) and (b) for comparison with our results (Fig. S1 (c) and (d)).

We have calculated the permittivity tensor of monolayer graphene and *h*-boron nitride by the density functional theory in the generalized gradient approximation (GGA) using the optical package of SIESTA. A Kgrid-Monkhorst-Pack mesh of $250 \times 250 \times 1$ and a 300 Ry energy cutoff are used to ensure converged GGA results. In order to fulfill the *f*-sum rule, it is necessary to set

the energy range 0-40 eV or even wider. An optical mesh of $800 \times 800 \times 4$ is used, which determines the mesh size used for the integration across the Brillouin zone related to the calculation accuracy.

We can see from Fig. S1 that they match very well in the frequency band of interest, 4.3-6.5 eV. Noticeable deviation happens only near some anomalous resonances which are not important in our manuscript. The source of error is the difference of accuracy including optical mesh, pseudopotentials, orbital basis sets, and optical energy range in different methods.

Optical properties of multilayer graphene

We have calculated the dielectric tensors of graphene from one layer to six layers and graphite for different polarized waves which are showed in Fig. S2. From which we can see that there are indeed some differences in the dielectric constants with the thickness increase of multi-layer graphene, but these differences mostly locate out of the ultraviolet spectrum and below 1200 THz (we use 1200 THz and 1400 THz for our design). This is because the coupling between layers mainly affect low-energy range which is much less than 1200 THz. Therefore, for the ultraviolet frequency range, the coupling effects are not significant. In addition, it needs to be emphasized that the impact of the interaction between layers is relatively small to ϵ_{\perp} with electric field perpendicular to optic axis, as is shown in Fig. S3(a-d). While, for ϵ_{\parallel} with electric field parallel to the optic axis, relatively large difference values are found between different layers.

The derivation of hyperbolic dispersion curve

By using the *k*DB system in Ref. [S1], we have given the details of derivation as follows:
For an anisotropic material with

$$\bar{\varepsilon} = \begin{bmatrix} \varepsilon_x & 0 & 0 \\ 0 & \varepsilon_y & 0 \\ 0 & 0 & \varepsilon_z \end{bmatrix}, \quad \bar{\mu} = \begin{bmatrix} \mu_x & 0 & 0 \\ 0 & \mu_y & 0 \\ 0 & 0 & \mu_z \end{bmatrix}, \quad (1)$$

their inverses are

$$\bar{\kappa} = \begin{bmatrix} 1/\varepsilon_x & 0 & 0 \\ 0 & 1/\varepsilon_y & 0 \\ 0 & 0 & 1/\varepsilon_z \end{bmatrix}, \quad \bar{\nu} = \begin{bmatrix} 1/\mu_x & 0 & 0 \\ 0 & 1/\mu_y & 0 \\ 0 & 0 & 1/\mu_z \end{bmatrix}. \quad (2)$$

Firstly, we need the transmission matrix to transform the quantities from Cartesian coordinate system to the k DB system. The transmission matrix defined in Ref. [S1] is

$$\bar{\bar{T}} = \begin{bmatrix} \sin \phi & -\cos \phi & 0 \\ \cos \theta \cos \phi & \cos \theta \sin \phi & -\sin \theta \\ \sin \theta \cos \phi & \sin \theta \sin \phi & \cos \theta \end{bmatrix}, \quad (3)$$

and its inverse is

$$\bar{\bar{T}}^{-1} = \begin{bmatrix} \sin \phi & \cos \theta \cos \phi & \sin \theta \cos \phi \\ -\cos \phi & \cos \theta \sin \phi & \sin \theta \sin \phi \\ 0 & -\sin \theta & \cos \theta \end{bmatrix}, \quad (4)$$

$$\bar{\bar{\kappa}}_k = \bar{\bar{T}} \cdot \bar{\kappa} \cdot \bar{\bar{T}}^{-1}$$

$$= \begin{bmatrix} \frac{\sin^2 \phi + \cos^2 \phi}{\varepsilon_x} & \frac{\cos \theta \sin \phi \cos \phi}{\varepsilon_x} - \frac{\cos \theta \sin \phi \cos \phi}{\varepsilon_y} & \frac{\sin \theta \sin \phi \cos \phi}{\varepsilon_x} - \frac{\sin \theta \sin \phi \cos \phi}{\varepsilon_y} \\ \frac{\cos \theta \sin \phi \cos \phi}{\varepsilon_x} - \frac{\cos \theta \sin \phi \cos \phi}{\varepsilon_y} & \frac{\cos^2 \theta \cos^2 \phi}{\varepsilon_x} + \frac{\cos^2 \theta \sin^2 \phi}{\varepsilon_y} + \frac{\sin^2 \theta}{\varepsilon_z} & \frac{\sin \theta \cos \theta \cos^2 \phi}{\varepsilon_x} + \frac{\sin \theta \cos \theta \sin^2 \phi}{\varepsilon_y} - \frac{\sin \theta \cos \theta}{\varepsilon_z} \\ \frac{\sin \theta \sin \phi \cos \phi}{\varepsilon_x} - \frac{\sin \theta \sin \phi \cos \phi}{\varepsilon_y} & \frac{\sin \theta \cos \theta \cos^2 \phi}{\varepsilon_x} + \frac{\sin \theta \cos \theta \sin^2 \phi}{\varepsilon_y} - \frac{\sin \theta \cos \theta}{\varepsilon_z} & \frac{\sin^2 \theta \cos^2 \phi}{\varepsilon_x} + \frac{\sin^2 \theta \sin^2 \phi}{\varepsilon_y} + \frac{\cos^2 \theta}{\varepsilon_z} \end{bmatrix}$$

$$(5)$$

$$\bar{\bar{\nu}}_k = \bar{\bar{T}} \cdot \bar{\nu} \cdot \bar{\bar{T}}^{-1}$$

$$= \begin{bmatrix} \frac{\sin^2 \phi + \cos^2 \phi}{\mu_x} & \frac{\cos \theta \sin \phi \cos \phi}{\mu_x} - \frac{\cos \theta \sin \phi \cos \phi}{\mu_y} & \frac{\sin \theta \sin \phi \cos \phi}{\mu_x} - \frac{\sin \theta \sin \phi \cos \phi}{\mu_y} \\ \frac{\cos \theta \sin \phi \cos \phi}{\mu_x} - \frac{\cos \theta \sin \phi \cos \phi}{\mu_y} & \frac{\cos^2 \theta \cos^2 \phi}{\mu_x} + \frac{\cos^2 \theta \sin^2 \phi}{\mu_y} + \frac{\sin^2 \theta}{\mu_z} & \frac{\sin \theta \cos \theta \cos^2 \phi}{\mu_x} + \frac{\sin \theta \cos \theta \sin^2 \phi}{\mu_y} - \frac{\sin \theta \cos \theta}{\mu_z} \\ \frac{\sin \theta \sin \phi \cos \phi}{\mu_x} - \frac{\sin \theta \sin \phi \cos \phi}{\mu_y} & \frac{\sin \theta \cos \theta \cos^2 \phi}{\mu_x} + \frac{\sin \theta \cos \theta \sin^2 \phi}{\mu_y} - \frac{\sin \theta \cos \theta}{\mu_z} & \frac{\sin^2 \theta \cos^2 \phi}{\mu_x} + \frac{\sin^2 \theta \sin^2 \phi}{\mu_y} + \frac{\cos^2 \theta}{\mu_z} \end{bmatrix}$$

$$(6)$$

Since we only consider the TM wave in the paper, we can simplify the calculation process.

$$\underline{\underline{\kappa}}_k = \begin{bmatrix} \frac{1}{\epsilon_y} & 0 & 0 \\ 0 & \frac{\cos^2 \theta + \sin^2 \theta}{\epsilon_x} - \frac{\sin \theta \cos \theta}{\epsilon_z} & \frac{\sin \theta \cos \theta}{\epsilon_x} - \frac{\sin \theta \cos \theta}{\epsilon_z} \\ 0 & \frac{\sin \theta \cos \theta}{\epsilon_x} - \frac{\sin \theta \cos \theta}{\epsilon_z} & \frac{\sin^2 \theta + \cos^2 \theta}{\epsilon_x} + \frac{\cos^2 \theta}{\epsilon_z} \end{bmatrix}, \quad (7)$$

$$\underline{\underline{\nu}}_k = \begin{bmatrix} \frac{1}{\mu_y} & 0 & 0 \\ 0 & \frac{\cos^2 \theta + \sin^2 \theta}{\mu_x} - \frac{\mu_z}{\mu_z} & \frac{\sin \theta \cos \theta}{\mu_x} - \frac{\sin \theta \cos \theta}{\mu_z} \\ 0 & \frac{\sin \theta \cos \theta}{\mu_x} - \frac{\sin \theta \cos \theta}{\mu_z} & \frac{\sin^2 \theta + \cos^2 \theta}{\mu_x} + \frac{\cos^2 \theta}{\mu_z} \end{bmatrix}, \quad (8)$$

From the Maxwell equations within the frame of the *k*DB system, we can get a matrix form between D and B at different directions as below

$$\begin{bmatrix} \kappa_{11} & \kappa_{12} \\ \kappa_{21} & \kappa_{22} \end{bmatrix} \cdot \begin{bmatrix} D_1 \\ D_2 \end{bmatrix} = \begin{bmatrix} 0 & u \\ -u & 0 \end{bmatrix} \cdot \begin{bmatrix} B_1 \\ B_2 \end{bmatrix}, \quad \begin{bmatrix} \nu_{11} & \nu_{12} \\ \nu_{21} & \nu_{22} \end{bmatrix} \cdot \begin{bmatrix} B_1 \\ B_2 \end{bmatrix} = \begin{bmatrix} 0 & -u \\ u & 0 \end{bmatrix} \cdot \begin{bmatrix} D_1 \\ D_2 \end{bmatrix}, \quad (9)$$

From Eq. (5) and Eq. (6), we can get

$$\begin{bmatrix} \frac{1}{\epsilon_y} - u^2 \frac{1}{\cos^2 \theta + \sin^2 \theta} & 0 \\ \frac{\mu_x}{\mu_x} & \frac{\cos^2 \theta + \sin^2 \theta - u^2 \mu_y}{\epsilon_z} \end{bmatrix} \cdot \begin{bmatrix} D_1 \\ D_2 \end{bmatrix} = 0, \quad (10)$$

For TM wave $D_1 = 0$ and $u = \omega/k$, the dispersion relations in anisotropic materials are given by

$$\frac{k_z^2}{\epsilon_x} + \frac{k_x^2}{\epsilon_z} = \omega^2 \mu_y. \quad (11)$$

If ϵ_x and ϵ_z has different signs, then the dispersive curve is hyperbolic.

Calculation process of flat hyperlens transmission

Consider a TM plane wave with $\hat{\vec{k}}_i = \hat{x} k_{ix} + \hat{z} k_{iz}$ incident from Region 0 as described in Fig. 2(a) in the manuscript. The total electric and magnetic fields are expressed as follows:

In Region 0:

$$\overline{H_0} = \hat{y}(e^{ik_{iz}z} + R^{TM}e^{-ik_{iz}z}) \cdot e^{ik_x x}, \quad (1)$$

$$\overline{E_{0x}} = \frac{\hat{x}k_{iz}}{\omega\epsilon_0} (e^{ik_{iz}z} - R^{TM}e^{-ik_{iz}z}) \cdot e^{ik_x x}, \quad (2)$$

$$\overline{E_{0z}} = \frac{-\hat{z}k_x}{\omega\epsilon_0} (e^{ik_{iz}z} + R^{TM}e^{-ik_{iz}z}) \cdot e^{ik_x x}, \quad (3)$$

In Region 1:

$$\overline{H_1} = \hat{y}(Ae^{ik_{1z}z} + Be^{-ik_{1z}z}) \cdot e^{ik_x x}, \quad (4)$$

$$\overline{E_{1x}} = \frac{\hat{x}k_{1z}}{\omega\epsilon_x} (Ae^{ik_{1z}z} - Be^{-ik_{1z}z}) \cdot e^{ik_x x}, \quad (5)$$

$$\overline{E_{1z}} = \frac{-\hat{z}k_x}{\omega\epsilon_z} (Ae^{ik_{1z}z} + Be^{-ik_{1z}z}) \cdot e^{ik_x x}, \quad (6)$$

In Region 2:

$$\overline{H_2} = \hat{y}T^{TM}e^{ik_{2z}z} \cdot e^{ik_x x}, \quad (7)$$

$$\overline{E_{2x}} = \frac{\hat{x}T^{TM}k_{2z}}{\omega\epsilon_0} e^{ik_{2z}z} e^{ik_x x}, \quad (8)$$

$$\overline{E_{2z}} = \frac{-\hat{z}T^{TM}k_x}{\omega\epsilon_0} e^{ik_{2z}z} e^{ik_x x}, \quad (9)$$

The coefficients R, A, B, and T can be found by matching the boundary conditions for the tangential electric and magnetic fields with T expressed as

$$T = \frac{\overline{H_2}(z=d)}{\overline{H_0}(z=0)} = \frac{4e^{i(k_{1z}-k_{2z})d}}{(1+p_{01}) \cdot (1+p_{12}) + (1-p_{01}) \cdot (1-p_{12})e^{i2k_{1z}d}}, \quad (10)$$

where

$$p_{01} = \frac{\epsilon_0 k_{1z}}{\epsilon_z k_{iz}}, \quad p_{12} = \frac{\epsilon_z k_{2z}}{\epsilon_0 k_{1z}}.$$

The time-averaged power density for TM wave can be expressed as

$$\langle S_n \rangle = \frac{1}{2} \operatorname{Re} \left\{ \overline{E}_n \times \overline{H}_n^* \right\}, \quad (11)$$

where $n = 0, 1, 2$ represent Region 0, 1, and 2, respectively. Ref. [S1] shows that the direction of time-average Poynting's vector is normal to the tangent of the k -surface. The theoretical derivation of hyperlens was shown in Ref. [S6,S7]. When $\varepsilon_z < 0$ and ε_x is positive, hyperbolic curve in Fig. 2(b) in the manuscript can be nearly parallel to the k_x axis. The time-average Poynting's vector for all the waves with different k_x component will be approximately perpendicular to x axis, indicating a highly directive propagation. Electromagnetic waves in anisotropic medium with different signs of dielectric constant have high directivity of $\langle S_1 \rangle$ so that two close point sources can be distinguished in the far field.

Silver based flat superlens/hyperlens compared with layered graphene

Previous superlens/hyperlens implementations usually adopted metal (Silver in Ref. [S8]) or metal/dielectric layers (Silver and Al_2O_3 in Ref. [S9]) to image sub-diffraction-limited objects at optical frequencies. Here we give the comparison of silver based flat superlens/hyperlens with graphene hyperlens at 1200 THz to confirm that at this frequency, silver based superlens/hyperlens dose not possess subwavelength imaging capabilities. Figure S3 shows the simulation results of flat hyperlens based on layered graphene, silver superlens and hyperlens based on silver with Aluminum Oxide (Al_2O_3). The thickness of flat hyperlens is 70 nm and two sources located along x-axis with distance of 70 nm. Figure S3(a) showed the H_y field distribution with layered graphene based flat hyperlens with $\varepsilon_z = -3.817 + 4.265i$ and $\varepsilon_x = 2.229 + 0i$, (b) and (c) are H_y field distribution with silver only and silver ($\varepsilon = -0.213 + 3.639i$ at 1200 THz [S10]) with Aluminum Oxide ($\varepsilon = 3.24 + 0i$ at 1200 THz [S11]) respectively. Figure S3(d) is the

comparison of the intensity in the image plane for layered graphene, silver only and silver/Al₂O₃, respectively. It is clear to see that at a high frequency such as 1200 THz, silver based superlens/hyperlens cannot work well.

Silver based cylindrical superlens/hyperlens compared with graphene based hyperlens

Figure S4 presents the comparison of the simulation results of cylinder hyperlens based on layered graphene and silver/Al₂O₃ at 1200 THz. From Fig. S4(a) we can see that although ε_z has an imaginary part ($\varepsilon_z = -3.817 + 4.086i$) comparable to silver ($\varepsilon = -0.213 + 3.639i$), the diffraction limit also can be overcome because the loss introduced by the imaginary part of ε_z is very limited in the wave propagation in the radial direction. However, the silver/Al₂O₃ based hyperlens showed in Fig. S4(b) has no hyperlens effect at all and energy attenuated very fast. It is the superiority of layered graphene.

SUPPLEMENTARY REFERENCE

- [S1] J. A. Kong, (EMW Publishing, Cambridge, Massachusetts, USA, **2008**).
- [S2] P. E. Blöchl, *Phys. Rev. B*, 1994, **50**, 17953.
- [S3] J. P. Perdew, K. Burke and M. Ernzerhof, *Phys. Rev. Lett.*, 1996, **77**, 3865.
- [S4] H. J. Monkhorst and J. D. Pack, *Phys. Rev. B*, 1976, **13**, 5188..
- [S5] P. B. Johnson and R. W. Christy, *Phys. Rev. B*, 1972, **6**, 4370.
- [S6] A. Salandrino and N. Engheta, *Phys. Rev. B*, 2006, **74**, 075103.
- [S7] Z. Jacob, L. V. Alekseyev, and E. Narimanov, *Opt. Express*, 2006, **14**, 8247.
- [S8] N. Fang, H. Lee, C. Sun and X. Zhang, *Science*, 2005, **308**, 534.

- [S9] Z. Liu, H. Lee, Y. Xiong, C. Sun, and X. Zhang, *Science*, 2007, **315**, 1686.
- [S10] P. B. Johnson and R. W. Christy, *Phys. Rev. B*, 1972, **6**, 4370.
- [S11] R. H. French, H. Mullejans, and D. J. Jones, *J. Am. Ceram. Soc.*, 1998, **81**, 2549.

SUPPLEMENTARY FIGURES

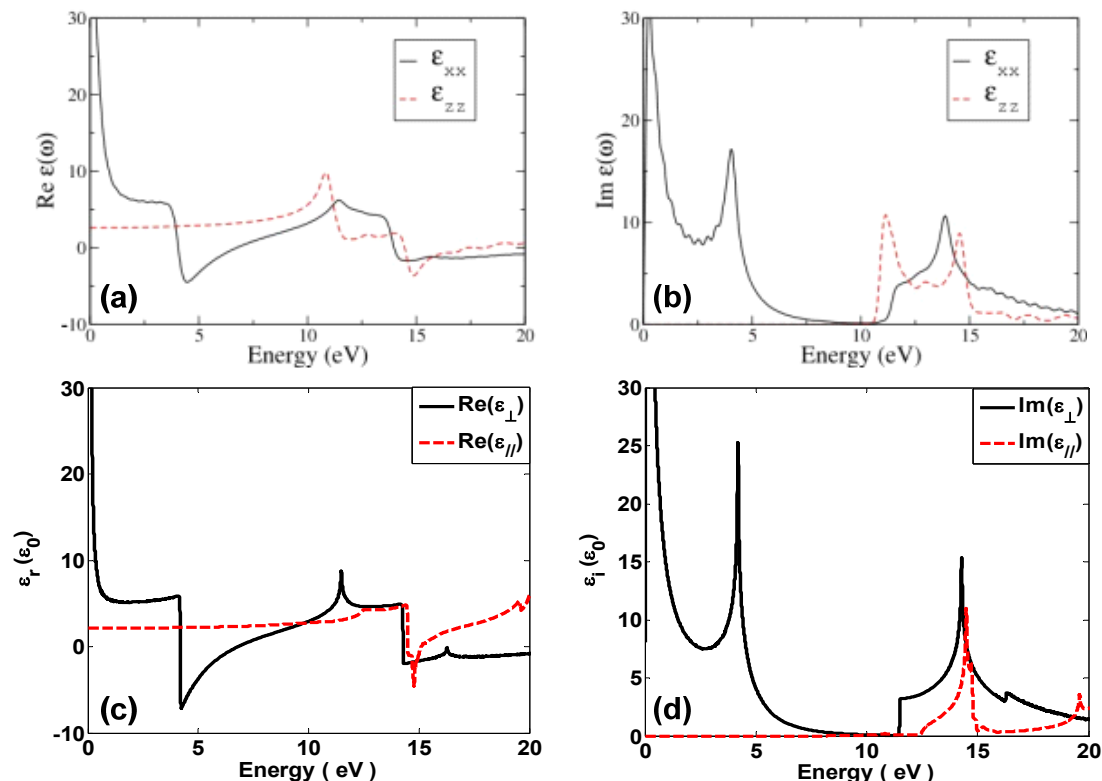
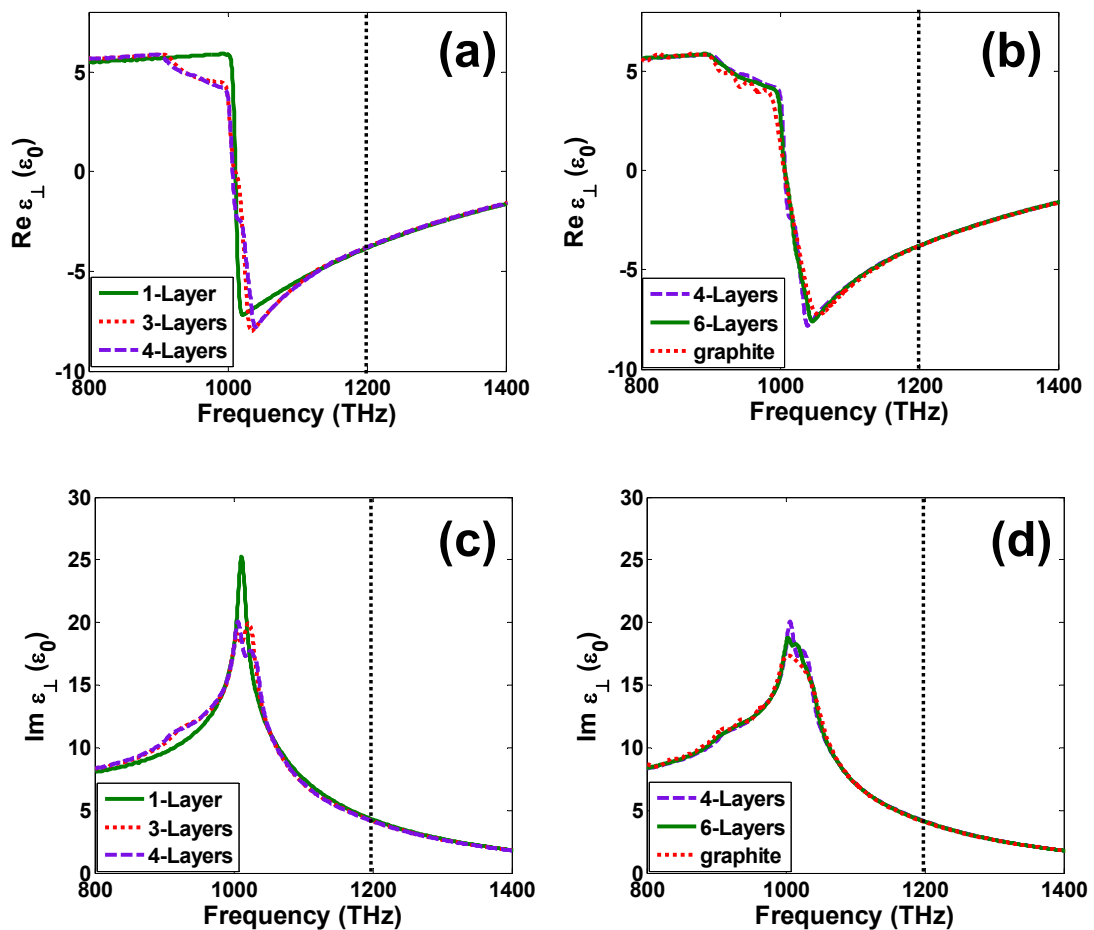


Fig. S1: Real (left) and imaginary (right) part of the dielectric function of monolayer graphene.

The x -component (ϵ_{xx} or ϵ_{\perp}) presented in black lines are the dielectric tensor for electric field perpendicular to the optic axis, the dielectric tensor for electric field parallel to the optic axis (ϵ_{zz} or $\epsilon_{||}$) are presented in red lines. The results calculated by M Klintenberg et al. in Ref. [17] (Copyright 2012 J. Phys.: Condens. Matter) are shown in (a,b) while (c) and (d) are our results. Results in Fig. S1 show that our calculation agrees with previous publications.



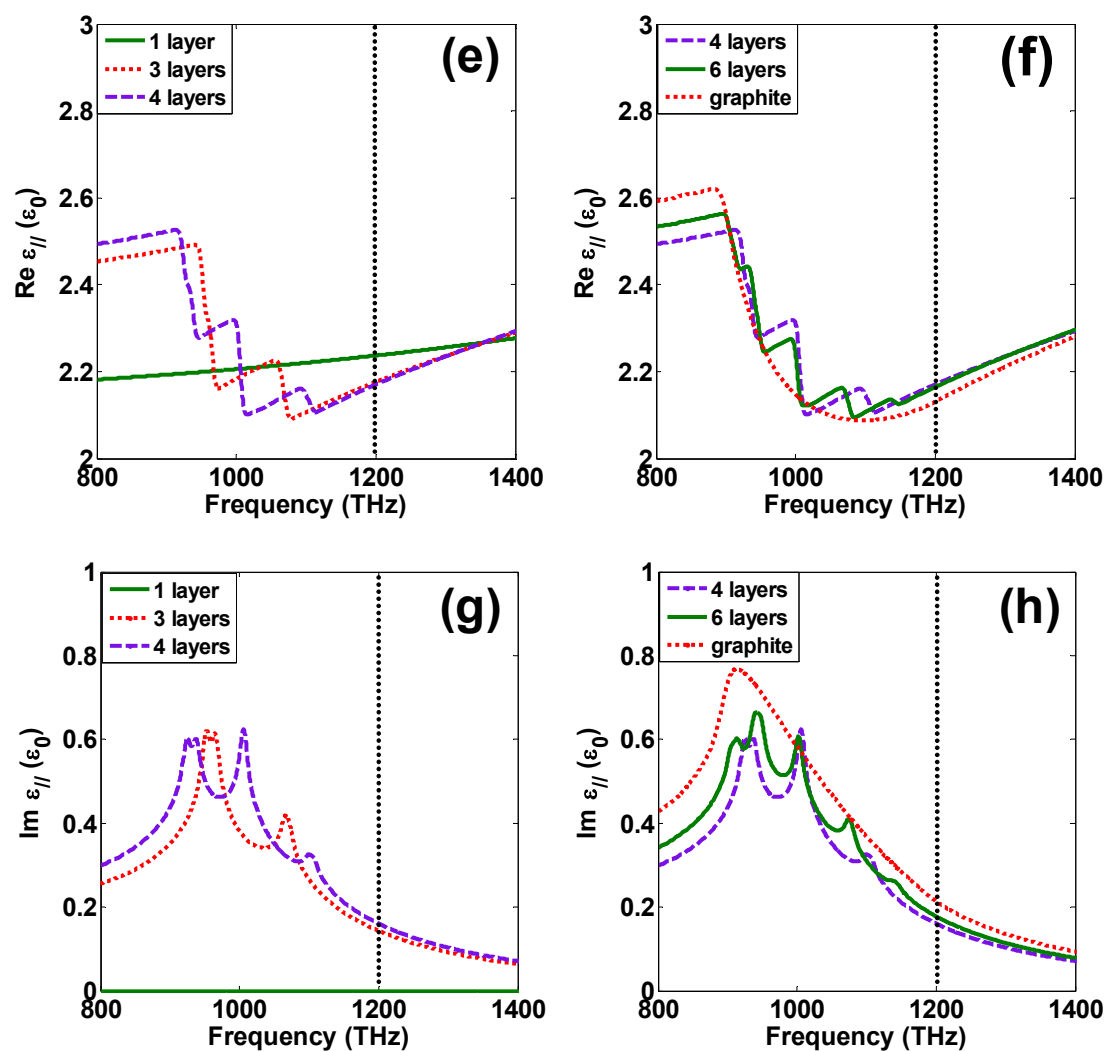


Fig. S2: Dielectric tensors of graphene from one layer to six layers and graphite for different polarized waves. The real part of permittivity for waves with electric field perpendicular and parallel to the optic axis are showed in (a,b,e,f) respectively. (c,d,g,h) are the corresponding imaginary parts of dielectric tensors.

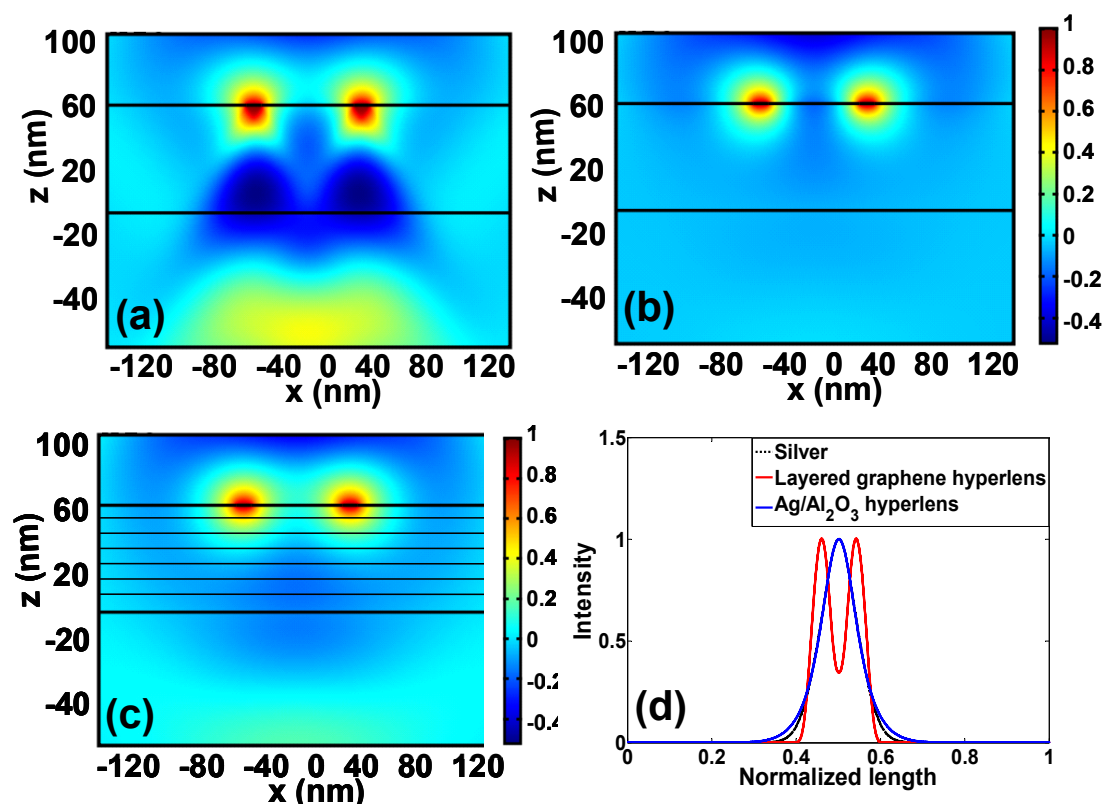


Fig. S3: Simulation results of planar hyperlens based on graphene at frequency of 1200 THz compared to silver based superlens and stack structure of silver and Aluminum Oxide(Al_2O_3). (a) H_y field distribution with layered graphene based flat hyperlens with $\varepsilon_z = -3.817 + 4.265i$ and $\varepsilon_x = 2.229 + 0i$, the thickness of this flat hyperlens is 70 nm, two sources located along x-axis with the distance about 70 nm; (b) H_y field distribution with silver in the inner rectangular with $\varepsilon = -0.213 + 3.639i$ at 1200 THz; (c) H_y field distribution with stack of silver (10 nm) and Al_2O_3 (10 nm); (d) the comparison of the average energy flow in the image plane for layered graphene, silver only and silver/ Al_2O_3 , respectively.

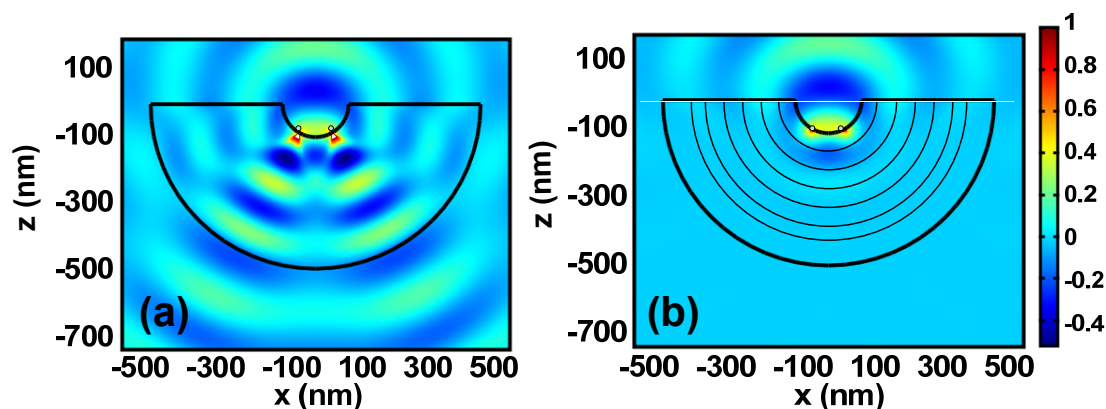


Fig. S4: Simulation results of cylindrical hyperlens based on layered graphene and stack of layered silver/Aluminum Oxide for comparison at 1200 THz. The thickness of cylinder hyperlens is 400 nm and two sources are separated about 100 nm which is less than half of wavelength.